MATERIALS SCIENCE

Flexoelectric manipulation of ferroelectric polarization in self-strained tellurium

Yan Yan[1]†, Xiongyi Liang[1,2,3]†, Liqiang Wang[4]†, Yuxuan Zhang[1], Jiaming Zhou[5], Weijun Wang[1], Zhibo Zhang[4], Yu Zhou[6], Irum Firdous[4], Zhengxun Lai[7], Wei Wang[1], Pengshan Xie[1], Yuecheng Xiong[8], Walid A. Daoud[4], Zhiyong Fan[6], Dong-Myeong Shin[5], Yong Yang[4], Yang Lu[5]*, Xiao Cheng Zeng[1,9]*, You Meng[7]*, Johnny C. Ho[1,2,10,11]*

Beyond conventional ferroelectric compounds, the realization of single-element ferroelectricity expands the scope of ferroelectric materials and diversifies polarization mechanisms. However, strategies for manipulating ferroelectric dipoles in elemental ferroelectrics remain underexplored, limiting their broader applications. Here, we introduce a universal flexoelectric manipulation strategy to tune the ferroelectric and piezoelectric polarization of one-dimensional self-strained tellurium (Te) ferroelectrics. A substantial flexoelectric field of 9.55 microcoulombs per square centimeter was observed in self-strained Te, inducing a polarization rotation of 18°, comparable to the typical 15° rotation in ferroelectric $PbTiO_3$ compounds. This substantial polarization rotation enhances ferroelectric coercivity by 165% and piezoelectric responses by 75% compared to unstrained Te. Moreover, the flexoelectric manipulation of ferroelectric polarization demonstrated improved energy harvesting performance at the device level, surpassing most existing counterparts. Our findings highlight the crucial role of flexoelectricity-ferroelectricity coupling in developing high-performance single-element electromechanical devices and ferroelectronics.

INTRODUCTION

Ferroelectrics are featured by their switchable and nonvolatile spontaneous polarization, capable of various applications such as nonvolatile memories, neuromorphic computing, and renewable energy harvesting (*1*–*4*). Typically, ferroelectricity is observed in compound materials or mixtures, such as perovskite oxides and metal chalcogenides. Recently, single-element ferroelectrics have attracted great attention due to their more straightforward composition and structure and more accessible synthesis techniques. Free from impurities, elemental segregation, or additional compounds, these single-element ferroelectrics provide advantages in terms of simplicity, purity, and stability compared to traditional compound ferroelectrics (*5*–*10*). Low-dimensional materials made of single elements are predicted to have ferroelectricity, such as group IV elements (e.g., graphene and Si) and group V elements (e.g., P, As, Sb, and Bi), especially some of them showcase the potential in unconventional sliding and Moiré ferroelectricity (*11*–*14*). For experimental progress, the two-dimensional (2D) Bi monolayer was observed with in-plane spontaneous polarization, whereas 1D Te nanowires hold out-of-plane ferroelectricity (*15*–*17*). However, elemental materials generally stabilize in nonpolar structures with high symmetry; therefore, the ordered ferroelectric dipoles seem difficult to align spontaneously. This hinders the appearance of significant ferroelectric responses and limits their practical applications in various fields.

Flexoelectricity is an electromechanical coupling effect between electrical polarization and inhomogeneous strain of solid-state materials. The flexoelectric-induced potential becomes pronounced when material dimensions are reduced to the nanoscale (*18*, *19*), thus having a strong ability to tailor the electrical properties of nanomaterials (*20*–*24*). For instance, in ferroelectric compounds, the flexoelectricity effect is used to mechanically write their ferroelectric domain (e.g., $BaTiO_3$ and $CaTiO_3$) (*25*, *26*), producing room-temperature ferroelectricity in centrosymmetric paraelectric materials (e.g., $SrTiO_3$ and Bi_2O_2Se) (*27*, *28*) and enhancing the ferroelectric coercivity (*19*, *29*). Nevertheless, the inhomogeneous strain fields used in those works mainly stem from specialized substrates or epitaxial conditions, limiting the tunability and scalability of flexoelectricity. Also, other approaches, like defect engineering and chemical substitution, may degrade the properties of ferroelectrics (*30*, *31*). Thus, a previously unidentified strategy that could overcome the limitations associated with strain engineering, defect engineering, and chemical substitutions is needed for flexoelectricity-ferroelectricity coupling.

In this study, we investigated the self-strained effect in elemental tellurium (Te) ferroelectrics synthesized via an ultrafast vapor growth strategy, with growth times as short as 1 min. Enhanced inversion-symmetry breaking in self-strained Te induced a substantial flexoelectric field of 9.55 μC cm^{-2}. This flexoelectric field resulted in a notable polarization rotation of 18°, comparable to the 15° rotation observed in $PbTiO_3$ ferroelectric thin films (*32*). The self-strained Te exhibited remarkable improvements in ferroelectric coercivity (165%) and piezoelectric coefficient (75%) compared to unstrained Te of the same thickness (40 nm). These enhancements are attributed

[1]Department of Materials Science and Engineering, City University of Hong Kong, Hong Kong SAR 999077, P.R. China. [2]Shenzhen Research Institute, City University of Hong Kong, Shenzhen 518057, China. [3]Chengdu Research Institute, City University of Hong Kong, Chengdu 610200, China. [4]Department of Mechanical Engineering, City University of Hong Kong, Hong Kong SAR 999077, P.R. China. [5]Department of Mechanical Engineering, The University of Hong Kong, Hong Kong SAR 999077, P.R. China. [6]Department of Electronic & Computer Engineering, Hong Kong University of Science and Technology, Kowloon, Hong Kong SAR, P.R. China. [7]Changsha Semiconductor Technology and Application Innovation Research Institute, College of Semiconductors (College of Integrated Circuits), Hunan University, Changsha 410082, China. [8]Department of Chemistry, City University of Hong Kong, Hong Kong SAR 999077, P.R. China. [9]Hong Kong Institute for Clean Energy, City University of Hong Kong, Hong Kong 999077, China. [10]State Key Laboratory of Terahertz and Millimeter Waves, City University of Hong Kong, Hong Kong SAR 999077, P.R. China. [11]Institute for Materials Chemistry and Engineering, Kyushu University, Fukuoka 816 8580, Japan.
*Corresponding author. Email: johnnyho@cityu.edu.hk (J.C.H.); youmeng2@cityu.edu.hk (Y.M.); xzeng26@cityu.edu.hk (X.C.Z.); ylu1@hku.hk (Y.L.)
†These authors contributed equally to this work.

to the ferroelectric polarization rotation (*33*–*35*). An in situ study using Te-based ferroelectric tunnel junctions (FTJs) demonstrated that flexoelectricity generated by externally applied force has a strong capacity to control spontaneous ferroelectric polarization. Leveraging this flexoelectricity-ferroelectricity coupling, self-strained Te–based flexible nanogenerators produced higher output power than their unstrained counterparts. Our research presents a powerful approach for optimizing the electrical properties of single-element ferroelectrics, thereby enriching their electromechanical applications.

RESULTS

Ferroelectricity enhancement in self-strained Te

The self-strained Te was synthesized using an ultrafast growth strategy catalyzed by Au (figs. S1 and S2). The minimum growth time is 1 min, and the synthesis temperature is low to 100°C (see Materials and Methods and table S1). The self-strained Te has a nanoneedle-like shape characterized by marked diameter dimension reduction along the *c* axis of Te (Fig. 1A). This dimension shrinking formed quickly generates growth dislocations, like screw dislocations or mixed dislocations, leading to a substantial internal strain gradient (i.e., self-strain) (*36*, *37*) (for detailed discussion, see Supplementary Note 1 and fig. S3). High-angle annular dark-field scanning transmission electron microscopy (HAADF-STEM) images (fig. S4 and crystal structure illustrations in fig. S5) show Te having a unique chiral lattice structure that inherently lacks centrosymmetry. This feature was also confirmed using angle-resolved second harmonic generation (SHG) spectroscopy, by which the polar plot of the out-of-plane SHG intensity demonstrates two-lobe symmetry (Fig. 1B), verifying the structure asymmetry, a key premise of the appearance of ferroelectricity. In addition, the SHG intensity of self-strained and unstrained Te is compared in fig. S6. A reduction in SHG intensity is observed in the self-strained Te, which may result from decreased nonlinear susceptibility caused by the self-strain. Notably, the multivalency nature of Te promotes the existence of both positive and negative charge centers, implying that Te is a viable candidate for elemental ferroelectricity (*14*, *17*). Furthermore, the actual conductivity of our Te nanoneedles was measured with different metal/Te/metal device channel lengths. On the basis of the transfer length method, the estimated resistivity of Te nanoneedles is found to be significantly larger than that of metal and semimetal and is comparable to typical semiconductors (see details in fig. S7). In this case, this noticeable resistive effect can induce a considerable voltage drop in the Te nanoneedle body and effectively suppress the current leakage, indicating the ability to realize ferroelectric switching by applying an electric field.

After that, dual ac resonance tracking-switching spectroscopy piezoelectric force microscopy (DART-SS PFM) was used to identify the out-of-plane ferroelectricity of self-strained Te (for detailed discussion, see Supplementary Note 2). The atomic force microscope (AFM) images in Fig. 1C show the surface morphology and height profile (along the black dotted line), in which different thicknesses (i.e., 10, 40, 70, 100, and 130 nm) from the body to tip were probed. The corresponding PFM phase hysteresis in Fig. 1D shows a distinct 180° phase difference and a clear butterfly-shaped amplitude loop, indicating the typical ferroelectric behavior of self-strained Te. The phase hysteresis curves measured at five different thicknesses are summarized in Fig. 1E, where the coercive field is inversely proportional to the thickness (detailed data shown in figs. S8 to S14). Besides, PFM was also used to map and control the local distribution of ferroelectric domains in self-strained Te at both tip and body parts. The ferroelectric domains at the tip areas can be fully switched in response to the applied opposite dc bias (e.g., negative or positive), demonstrating good correspondence with the morphology (fig. S15). We found that the ferroelectric domains in body areas only can be partially switched, in which the domains of the middle parts having a thicker thickness cannot be switched (fig. S16), indicating weak ferroelectric properties and even nonferroelectric, well in line with the point PFM measurement results (Fig. 1F and figs. S10 to S14). The phase mapping data further confirmed the ferroelectric nature of our self-strained Te. Notably, similar ferroelectric behaviors were also observed at the inclined edge of much wider Te nanowires and Te nanosheets (*16*).

The unstrained Te, including horizontally and vertically aligned nanostructures (figs. S17 to S20), was also synthesized for properties comparison. Its unstrained feature was revealed by high-resolution TEM (fig. S21) and geometrical phase analysis (GPA), where a negligible level of internal strain was confirmed (fig. S22). The scaling relationship between coercive field and thickness of unstrained Te is also determined by combining the PFM signals (fig. S23) and theoretical calculations (see Materials and Methods). Obviously, the coercive field of self-strained Te is larger than that of unstrained Te at the same thicknesses (Fig. 1F). Specifically, the out-of-plane piezoelectric coefficient (d_{33}) of self-strained (2.06 pm/V) is also more substantial than that of unstrained Te (1.21 pm/V) under the same conditions (figs. S24 and S25). We ascribe those enhanced ferroelectric and piezoelectric responses to polarization rotation induced by large internal inhomogeneous strain in self-strained Te, which triggers the inversion symmetry breaking and favors the charge redistribution.

Polarization rotation induced by the self-strained approach

To verify our assumption, the self-strained feature of Te was studied first. Raman spectra in Fig. 2A demonstrate an obvious blue shift in the A_1 and E_2 modes, whereas the E_1 transverse (TO) phonon mode remains unchanged as the probed position moves from the body to the tip. This can be explained by the presence of internal tensile strain, which decreases the bond angle (θ) and increases interplanar spacing (*d*) (fig. S26). Consequently, the vibration of the A_1 and E_2 modes is enhanced, whereas the vibration of the E_1-TO mode remains unaffected. This phenomenon aligns well with external forces applied perpendicular to the Te chain (*10*). Besides, density functional theory (DFT) calculations were used to simulate the ferroelectric characteristics under different strain conditions. Clearly, there is no charge transfer under unstrained conditions, whereas significant charge redistribution responds to tensile or compressive strain. This strain breaks the inversion symmetry, increasing upward or downward polarization (Fig. 2B) (for more discussions of DFT calculations, refer to Supplementary Note 3 and figs. S27 to S30).

Furthermore, cross-sectional HAADF-STEM was conducted at the body (Fig. 2, C and D, and figs. S31 and S32) and tip positions (Fig. 2, F and G, and fig. S33) from the same representative Te nanoneedle. The corresponding GPA images directly visualize the internal strain. The tip of self-strained Te exhibits substantially larger internal strain than the body region, corroborating the results from Raman spectra. Compared to the interfacial strain engineering achieved using specific substrates (e.g., $PbTiO_3$ on a $DyScO_3$ substrate), the self-strain effect in this work arises from growth dislocations induced by the ultrafast growth strategy, representing an internal

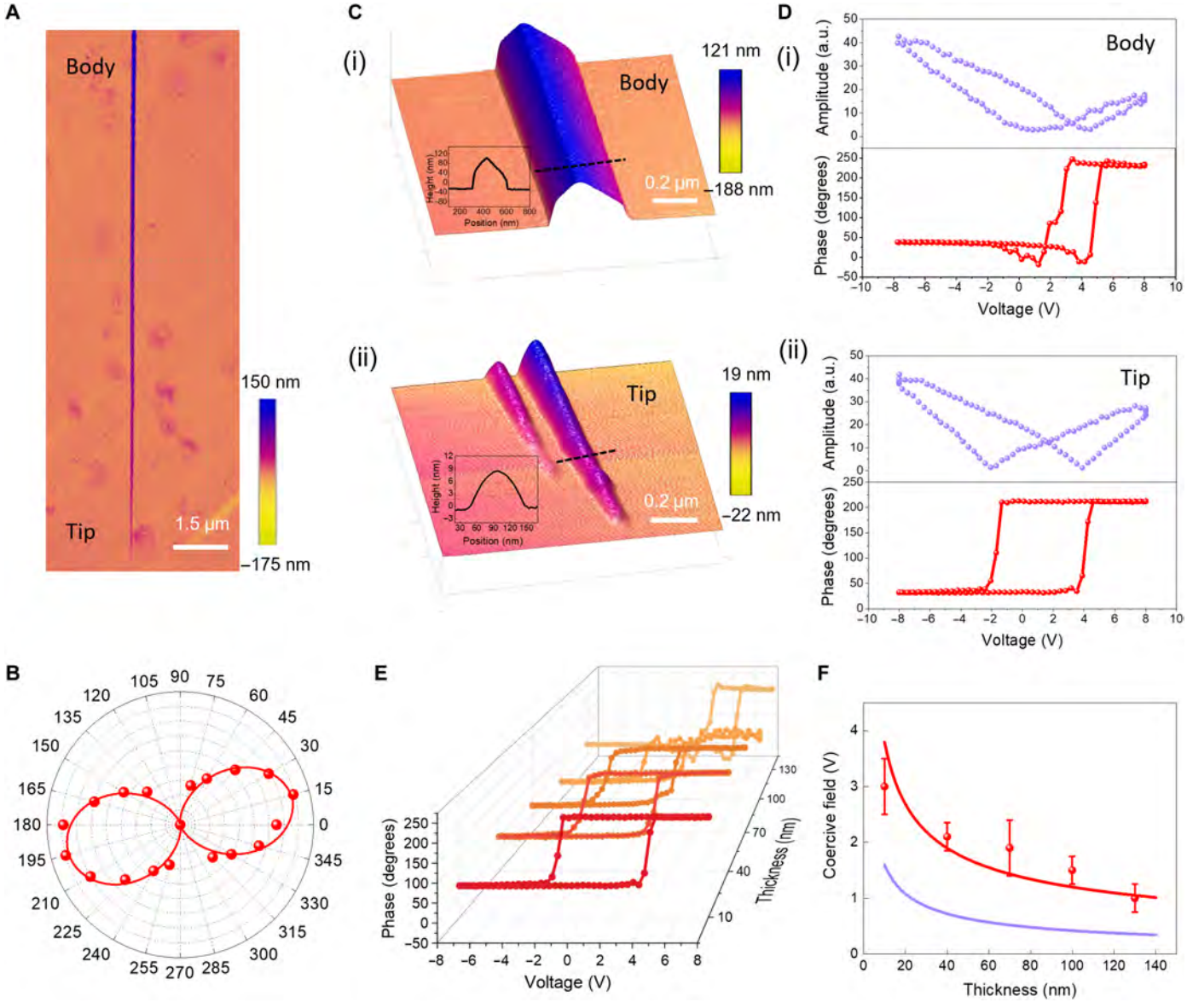

Fig. 1. Enhanced ferroelectricity in self-strained Te. (**A**) AFM morphology images of a typical self-strained Te with a needle-like shape. (**B**) SHG spectra of self-strained Te that verified the significant structure asymmetry of Te. (**C**) Enlarged AFM morphology of self-strained Te (i) at the body and (ii) at the tip positions. The inserted figure shows the height profile. (**D**) Off-field butterfly amplitude loop and phase hysteresis of self-strained Te (i) at the body and (ii) at the tip positions. a.u., arbitrary units. (**E**) Off-field phase hysteresis curves were measured at five different thicknesses (10, 40, 70, 100, and 130 nm) from the body to the tip. The coercive field experienced a notable enhancement when the AFM tip moved from the body to the tip. (**F**) Comparison of the scaling relationship between the coercive field and thickness of self-strained Te and unstrained Te.

bulk effect. Also, the internal strain is highly inhomogeneous and discontinuous, which would promote the polarization rotation (*23*, *32*). Moiré patterns were observed in some self-strained Te without any artificial stacking configurations (fig. S33), further highlighting the powerfulness of growth dislocations induced by the self-strain effect (for detailed analysis, see fig. S34 and Supplementary Note 1).

The strength of spontaneous polarization is linearly proportional to atomic displacement. The local polarization at the unit cell scale can be quantitatively assessed by measuring atomic displacement (figs. S35 and S36) (*38*–*40*). The polarization vector map can be obtained under different strain conditions (i.e., tensile, compressive, and unstrained). The maximum ferroelectric polarization, calculated based on experimental data, was 27.3 μC cm^{-2}, and this magnitude is in good agreement with the value of 26.9 μC cm^{-2} obtained from DFT computation (for details, see Supplementary Note 3). The average transverse flexoelectric polarization was determined as 9.55 μC cm^{-2} based on the relation $P_{\mathrm{Flexo}} \cong f_{13}\left(\Delta\varepsilon_3 / w\right)$, where f_{13} is the transverse flexoelectric coefficient, $\Delta\varepsilon_3$ is the out-of-plane strain, and w is the relaxation length (calculation details shown in Materials and Methods). The comparable values between the flexoelectric and spontaneous ferroelectric polarization were found in self-strained Te, suggesting the possibility of a flexoelectricity-ferroelectricity coupling effect. A maximum rotation angle (β) was calculated as 18° based on the equation $\tan\beta = P_{\mathrm{Flexo}} / P_{\mathrm{Ferro}}$, comparable to the rotated angle (15°)

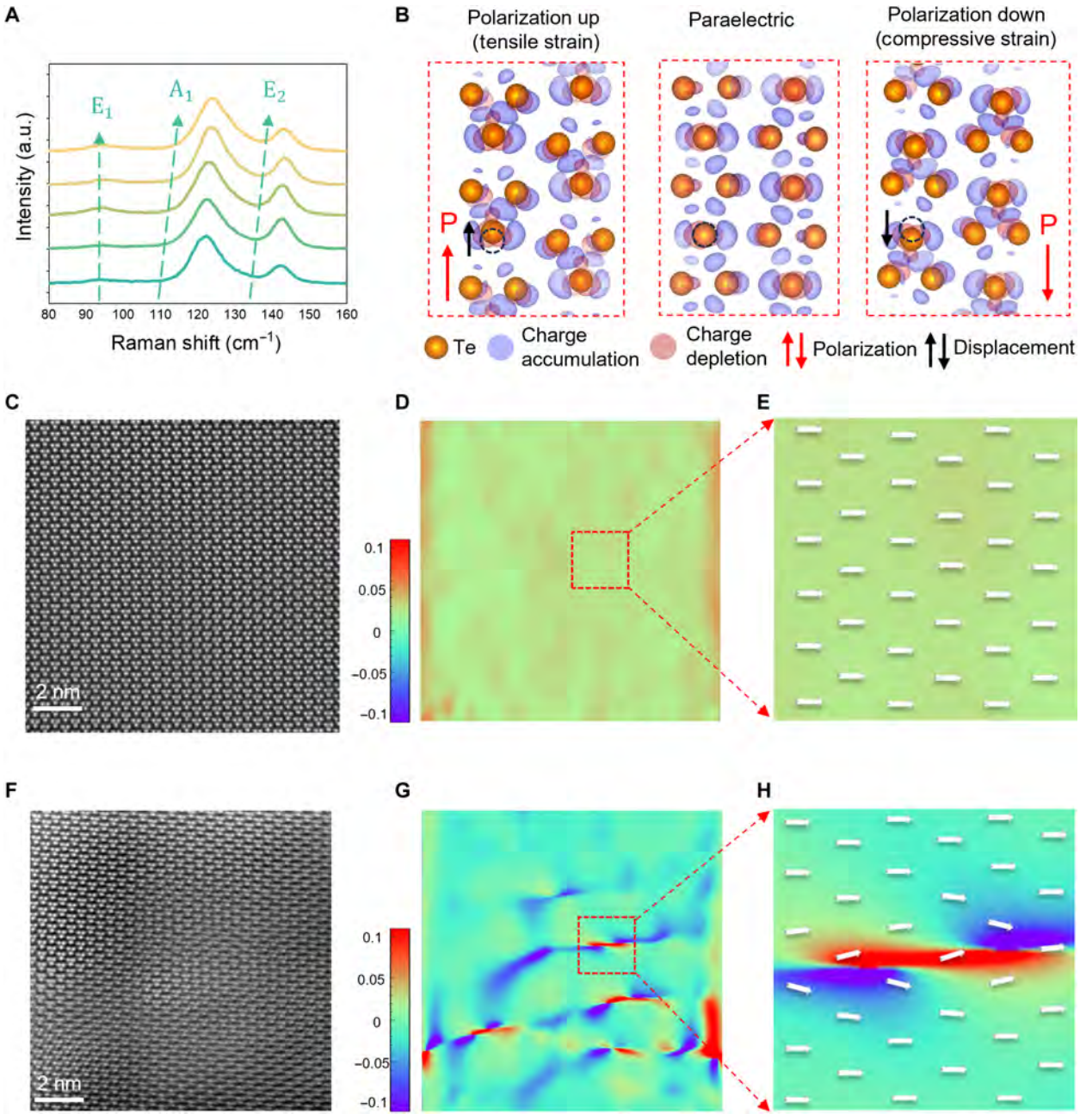

Fig. 2. Polarization rotation induced by the self-strained approach. (**A**) Raman spectra of self-strained Te indicating a substantial internal tensile strain. (**B**) Inversion symmetry, charge redistribution, and polarization rotation under different strain conditions. HAADF-STEM image and corresponding GPA (**C** and **D**) at the body position and (**F** and **G**) at the tip position. The polarization vector map of (**E**) the body and (**H**) the tip.

in $PbTiO_3$ ferroelectric thin film (*32*). This means the pronounced transverse flexoelectric polarization can partially rotate the longitudinal ferroelectric polarization. The polarization vector map illustrated in Fig. 2 (E and H) shows an apparent polarization rotation in response to internal inhomogeneous strain (for polarization vector mapping at a larger scale, see figs. S35 and S36). The displacement orientation and strain gradient are consistent. The rotation directions of spontaneous polarization in compressive and tensile nanoregions are contrary (e.g., upward direction at tensile nanoregions marked in red color in Fig. 2H, whereas the downward direction in blue color highlights compressive nanoregions) (for details, see fig. S37), confirming that polarization rotation is driven by flexoelectricity-ferroelectricity coupling.

Flexoelectric manipulation of ferroelectric polarization

Furthermore, to shed light on the capability of flexoelectricity in controlling ferroelectric polarization, an in situ FTJ study was conducted on self-strained Te with a 9–unit cell thickness (Fig. 3, A to

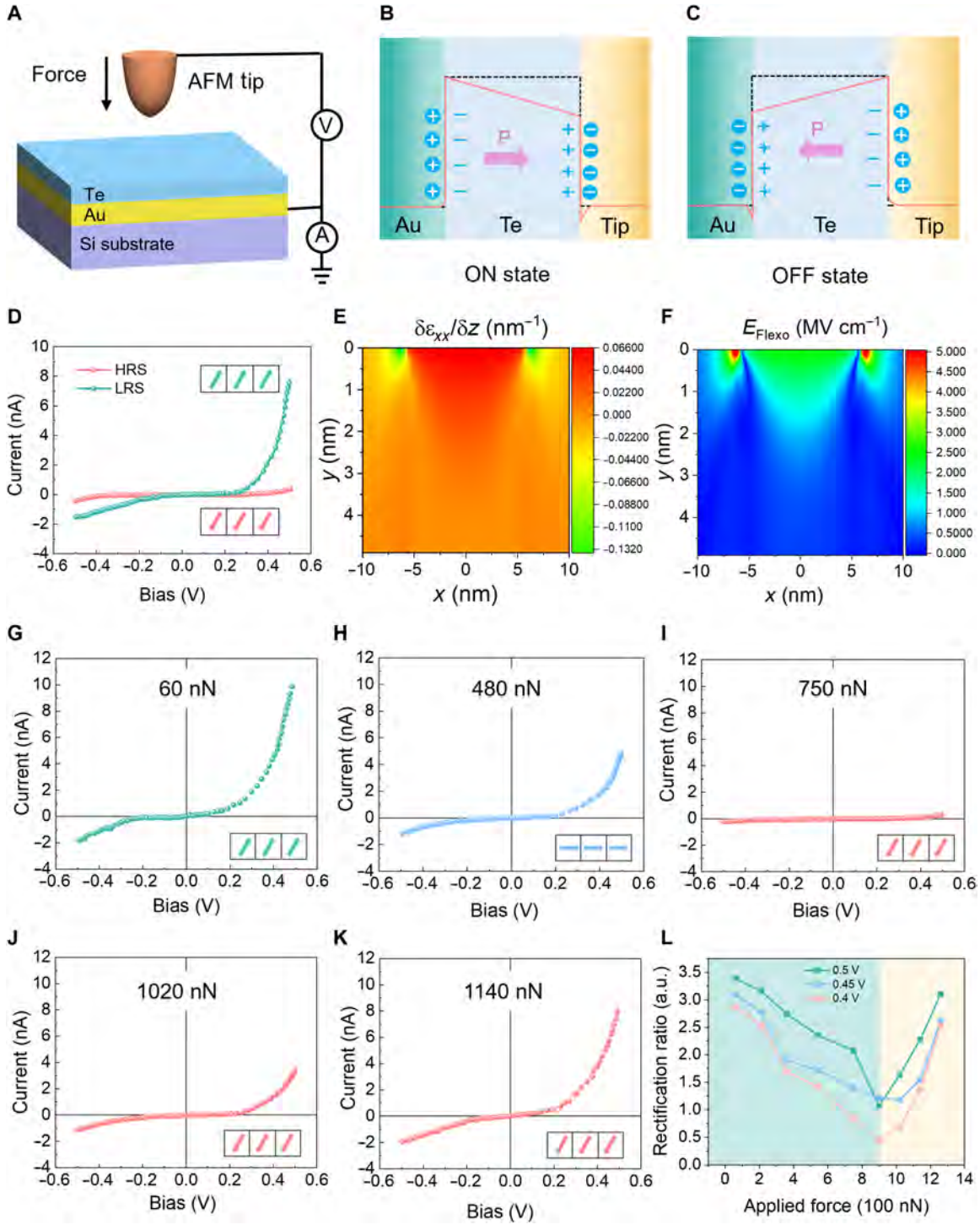

Fig. 3. Flexoelectric manipulation of polarization by external mechanical forces. (**A**) Structural illustration of self-strained Te–based M/F/M asymmetry FTJs. (**B** and **C**) The energy structures of Te-based FTJs are polarized in ON and OFF states. (**D**) *I-V* curves of Te-based FTJs responding to different applied biases (−3 or +3 V). (**E**) Inhomogeneous strain and the corresponding flexoelectric field distributed inside the Te barrier layer under an 800-nN force applied via the AFM tip. The operando *I-V* curves of Te-based FTJs measured at different applied forces of (**G**) 60 nN, (**H**) 480 nN, (**I**) 750 nN, (**J**) 1020 nN, and (**K**) 1140 nN. (**L**) Rectification ratios as a function of applied forces.

C). As the *I-V* curve of self-strained Te–based FTJs demonstrated in Fig. 3D, a distinct transition from low resistance state (LRS) to high resistance state (HRS) was observed after electrical poling (±5 V) that exceeds the coercive field. This suggests that the ferroelectric polarization direction switches from upward to downward, inducing the tunneling electroresistance effect (*41*, *42*). The ON/OFF ratio is ~50, comparable to the performance of other conventional ferroelectric material–based FTJs (e.g., $BaTiO_3$) (*41*, *42*).

Flexoelectricity generated by mechanical loads could alter the ferroelectric polarization of self-strained Te (*18, 43–45*). Using a tip-loaded method, the AFM tip was used to apply mechanical loads perpendicular to the Te chain; the generated strain and corresponding flexoelectric field were also simulated using the first-principles calculations (see Materials and Methods). Under a tip-loaded force of 800 nN, a pronounced 3D inhomogeneous strain up to 6.6×10^7 m^{-1} was observed in theoretical results (Fig. 3E and fig. S38), corresponding to a maximum flexoelectric field of 6.97 MV/cm (Fig. 3F). This field is large enough to break the local inversion symmetry, capable of switching local ferroelectric polarization and thereby modifying the FTJ conductance (*25*, *26*, *43*, *44*).

Furthermore, the strong ability of flexoelectricity in controlling spontaneous ferroelectric polarization was experimentally confirmed, reflected in the rectification ratios ($RR = |I_{+V}/I_{-V}|$, where I_{+V} and I_{-V} are the output current at opposing bias) of FTJs. Figure 3 (G to I) shows a clear transition from LRS to HRS and a decreasing rectification ratio when the applied force increased from 60 to 750 nN. Supported by the calculations, the strain-induced polarization reversal changes the mean barrier height by an amount of $\Delta\phi > 0.1$ eV, which is substantial enough to affect the tunneling current (details in Materials and Methods). This highlights the consistency between our experimental and theoretical results. Further increasing the applied force above 900 nN, the rectification ratios would show an increasing trend (Fig. 3, J and K, and fig. S39), and an LRS would be achieved again at an applied force of 1140 nN (Fig. 3K). This reversal phenomenon results from the strain-regulated interaction between barrier thickness and conduction band edge (*43*, *46*). The extracted rectification ratios as a function of applied forces are shown in Fig. 3L. At the same time, a similar trend was also witnessed in an 11–unit cell–thick Te-based FTJ, suggesting good repeatability (figs. S40 and S41). Given that even slight perturbation or instability from AFM facilities or the external environment can result in current fluctuation, we repeated those *I-V* curve measurements 40 times for self-strained and unstrained Te at various positions with similar thickness to further validate the reproducibility. The raw and average *I-V* curves are demonstrated in figs. S42 and S43, where good repeatability and operation stability were confirmed. The rectification ratios of the self-strained and unstrained Te-based FTJ were summarized in fig. S44, from which a higher rectification factor was observed from the self-strained Te–based FTJ compared with the unstrained Te-based counterpart, further indicating that the self-strained feature could favor the charge redistribution.

Enhanced energy harvesting performances

Flexoelectricity-ferroelectricity coupling uncovered in self-strained Te has the potential to develop high-performance electromechanical electronics. As a device-level demonstration, the flexible nanogenerators were fabricated with a typical sandwich structure of Au/Te/polymethyl methacrylate (PMMA)/Au (Fig. 4A), as verified in the cross-sectional scanning electron microscopy (SEM) images (fig. S45). In a control experiment, both self-strained and unstrained Te samples were used as the active layer of nanogenerators (Fig. 4B). First, Young's modulus of Te was measured as $E_r = 73.6$ GPa using the method of in situ uniaxial compression experiment (fig. S46), matching the simulation results (60.0 GPa) and comparable to other typical piezoelectric nanomaterials (table S2).

Responding to the applied periodic forces (illustrations inserted at the bottom of Fig. 4C), the nanogenerators based on self-strained Te generated stable peak voltage signals, in which the two distinct peaks with reverse polarity correspond to the compressing and releasing process (Fig. 4C). As supported by the COMSOL simulation, self-strained Te could output higher electric potential (Fig. 4D) and peak output voltage than unstrained Te (fig. S47) by nearly two and four times, respectively, under the same conditions. Under a periodic force of 85 N, the maximum output voltages from self-strained Te–based nanogenerators (2.40 V) are larger than those of unstrained vertical (1.75 V) and horizontal (0.42 V) Te-based devices, which aligns with the simulation results (Fig. 4E). The performance advantages of self-strained Te–based nanogenerators in terms of output voltage (Fig. 4F), accumulated charge (Fig. 4G), and output current (fig. S51) are witnessed under different mechanical periodic forces (for detailed data, refer to figs. S48 to S51). The enhanced performance of self-strained Te is attributed to the occurrence of polarization rotation induced by flexoelectricity when periodic forces are applied to the nanogenerator. Note that all the device outputs experience a monotonous increment with the applied forces, suggesting the reliable operation of Te-based nanogenerators (Fig. 4F and fig. S51).

Given the quasi-1D crystal structure, Te has intrinsic anisotropic mechanical properties (fig. S52 and table S3). On the basis of this, the outputs from vertical Te nanomaterial–based nanogenerator devices are notably larger than those of horizontal devices (Fig. 4, F and G, and fig. S51). The piezoelectric coefficients (d_{33}) were determined as 16.24 ± 1.59 and 3.57 ± 0.65 pC/N along the *c* axis and *a* axis of the Te crystal (Fig. 4G), respectively. Te's anisotropic energy harvesting ability could be used in intelligent electromechanical electronics, such as directional stress sensors and energy generators (*47*, *48*). These output voltage and piezoelectric coefficients of self-strained Te are comparable to those of typical piezoelectric nanomaterials, as summarized in Fig. 4H and table S4. Practically, the self-strained Te–based nanogenerators can easily power the commercial light-emitting diode (LED), with the LEDs alternating between on and off in response to periodic compressive forces, using only one nanogenerator (for details, see Supplementary Note 4, fig. S53, and movie S1). Furthermore, the piezoelectric potential generated by self-strained Te–based nanogenerators can effectively act as the gate voltage to stimulate the ion gel-gated synaptic transistor, triggering significant excitatory postsynaptic current (for details, see Supplementary Note 4, figs. S54 and S55, and movie S2). These demonstrations underscore the considerable application potential of self-strained Te–based nanogenerators in various fields, such as self-powered systems, artificial somatosensory systems, human health monitoring, etc.

DISCUSSION

In summary, we demonstrated the strong ability of flexoelectric manipulation of ferroelectric polarization in self-strained Te, leading to pronounced ferroelectric coercivity and piezoelectric responses. The self-strained effect enhances the inversion-symmetry breaking

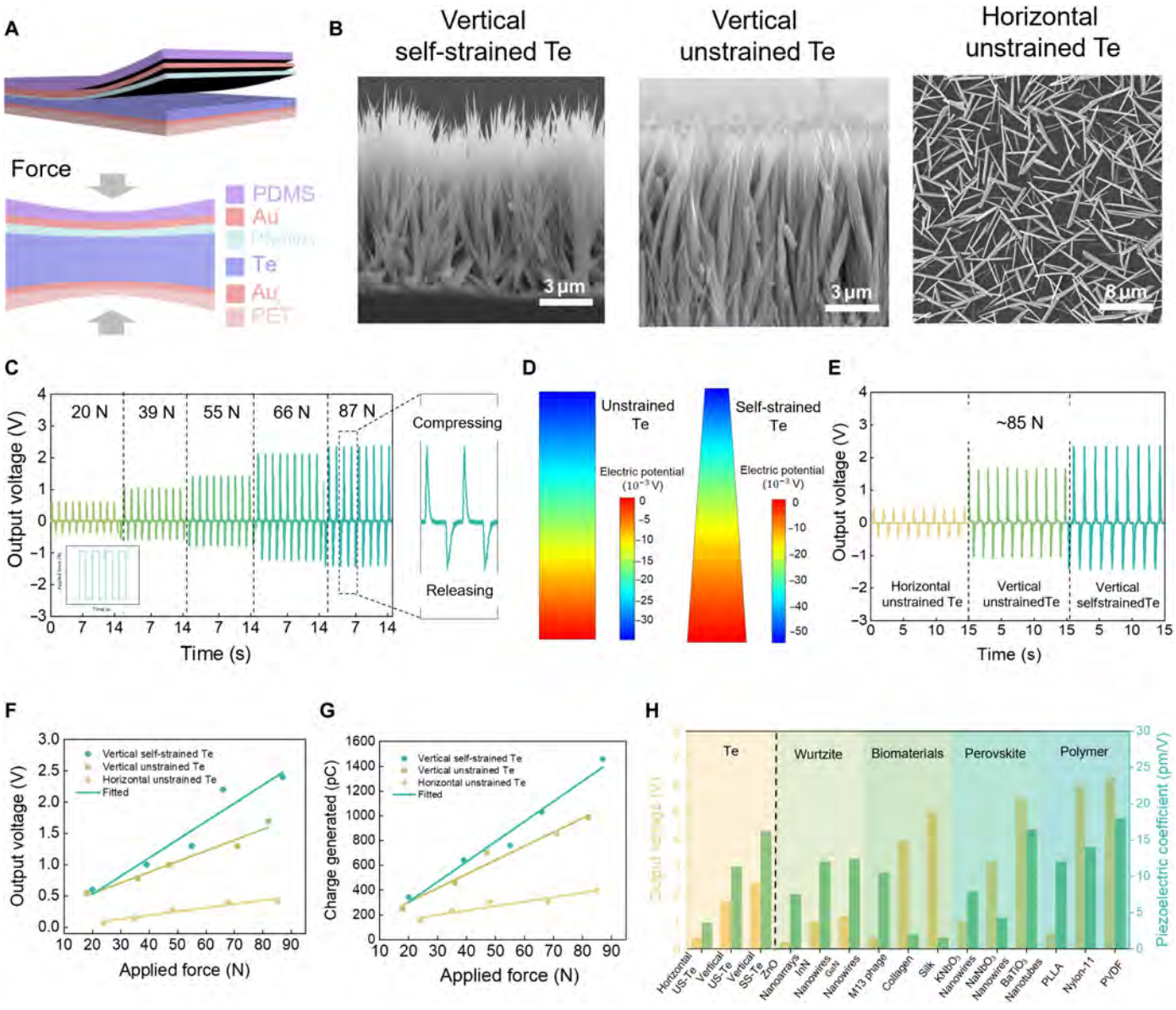

Fig. 4. Enhanced energy harvesting performances. (**A**) Structural illustration of a Te-based nanogenerator. (**B**) SEM images of three kinds of Te nanomaterials used in the nanogenerator. (**C**) Output voltages of the vertical self-strained Te–based nanogenerator as a function of applied forces. The inset on the right side shows two distinct output voltage peaks with a reverse polarity corresponding to the compressing and releasing process, and the inset below demonstrates the applied periodic forces. (**D**) COMSOL Multiphysics simulations of self-strained and unstrained Te at the same applied force. (**E**) Maximum output voltages of nanogenerators generated by three different kinds of Te nanomaterials. (**F**) Output voltage and (**G**) the accumulated charge as a function of applied forces. (**H**) Output voltage and piezoelectric coefficient of Te nanomaterials compared with other low-dimensional piezoelectric nanomaterials. US-Te, unstrained Te; SS-Te, self-strained Te; PLLA, poly-L-lactic acid; PVDF, polyvinylidene difluoride.

and favors the electric dipole alignment of chiral Te chains, by which a substantial increase in ferroelectric coercivity (165%) and piezoelectric coefficient (75%) was obtained. This self-strain approach overcomes limitations associated with specialized substrates, epitaxial conditions, and chemical substitution that may degrade the properties. Furthermore, the device-scale applicability of nanogenerators is demonstrated using self-strained Te, showing improved energy harvesting performance that surpasses most counterparts. On the basis of the quasi-1D Te crystal structure, Te's anisotropic energy harvesting ability was also demonstrated, promising for directional electromechanical electronics. Our work not only shows a feasible way to enhance and/or regulate the emerging single-element ferroelectricity but also provides a platform for the design of flexoelectricity-ferroelectricity coupled functional devices.

MATERIALS AND METHODS

Synthesis of Te nanomaterials

All Te nanomaterials were synthesized using the physical vapor deposition (PVD) method. The synthesis was conducted using a two-zone vapor transport system equipped with a 1-inch inner diameter quartz tube. In the high-temperature heating zone (500°C),

an alumina boat containing 1 g of Te powders (Aldrich, pieces, 99.999%) was placed to vaporize the precursor powders. The substrates, where the nanomaterials were to grow, were positioned in the low-temperature heating zone (100°C). Before the growth process, the system was evacuated, and an argon flow of 200 standard cubic centimeter per minute (SCCM) was introduced for 30 min to eliminate residual oxygen. To initiate growth, the vaporized Te was carried by an argon flow of 50 SCCM from the high-temperature zone to the low-temperature zone. The dimension and morphology of the different Te nanomaterials were controlled by adjusting the pressure, growth time, preannealing conditions, and catalysis. Horizontal self-strained Te and unstrained Te were synthesized at atmospheric pressure using a mica substrate without metal catalysis. In contrast, the vertically self-strained Te and unstrained Te were grown at 100 torr on a Au-coated silicon substrate. The Au served as the catalyst to boost the growth, effectively reducing the growth time. The Au-coated silicon substrate used for growing vertical self-strained Te and the mica substrate used for synthesizing horizontal self-strained Te were preannealed at 300°C for 20 min before growth. In contrast, the Au-coated silicon substrate used to synthesize vertical unstrained Te and the mica substrate for growing horizontal unstrained Te were not subjected to preannealing. The growth temperature for all Te nanomaterials was 100°C. The growth time was varied to control the diameter and length of all Te nanomaterials.

Characterizations of Te nanomaterials

The surface morphologies of the Te nanomaterials were characterized by optical microscopy, SEM (XL30, FEI/Philips ESEM-FEG), and AFM (Dimension Icon, Bruker). The Raman spectra were collected by a confocal microscope spectrometer (Alpha 300R, WITec). The crystal structures and crystallinity were examined by x-ray diffraction (D2 Phaser XE-T, Bruker). The SHG spectroscopy (Alpha 300R, WITec) was used to identify the structural asymmetry. TEM [high-resolution TEM (HRTEM), JEOL 2100F; HAADF-STEM, FEI-Titan Cubed Themis G2] was used to study the crystal structures at the atomic scale. The *I-V* curves of FTJs were measured using conductive AFM (CAFM) (MFP-3D infinity, Oxford) using a CAFM tip (ARROW-EFM, Nanoworld). The electrical bias was swiped from −0.5 to 0.5 V. Using a polymer-based wet-transfer method, all SEM, TEM, and CAFM samples were prepared by transferring Te samples onto a certain substrate (e.g., Si substrate for SEM, Cu grids for TEM, and Au-coated Si substrate for CAFM).

PFM measurements

Using a polymer-based wet-transfer method, the as-synthesized self-strained Te was first transferred to the Au-coated silicon substrate. The PFM (Dimension Icon of Bruker, and Cypher ES of Asylum Research) was used to obtain butterfly amplitude loop and phase hysteresis by sweeping the AC bias voltage from −3 to 3 V using a CAFM tip (SCM-PIT V2, Bruker). The PFM amplitude and phase signals provide insights into local electromechanical responses and differentiate various out-of-plane polarization orientations within a ferroelectric domain. Consequently, this allows for the direct observation of nanoscale ferroelectricity.

Mechanical properties of Te

The mechanical property of Te was studied from both theoretical and experimental aspects. The elastic tensor matrix was determined by DFT calculations and Young's modulus at both 3D spherical form and 2D projections on the (*xy*), (*xz*), and (*yz*) planes were directly visualized using ELATE (*49*). The magnitude of Young's modulus of Te along the *x*, *y*, and *z* axes was determined as 36, 36, and 60 GPa, respectively. Te demonstrated significant anisotropic properties, from which we can expect that the outputs from horizontal and vertical Te nanomaterials should be significantly different. Also, a quantitative nanoindentation system (Hysitron PI 85 PicoIndenter) equipped inside the SEM chamber (FEI Quanta 450 FESEM) was used to experimentally determine Young's modulus of vertical Te nanowires under displacement-control mode. The vertically unstrained Te directly grew on specialized Cu grids for nanoindentation. The mechanical force was applied using an indenter along the *c* axis of Te nanoneedles, whereas the feedback was monitored using pressure sensors, and the strain rate was at $\sim 2 \times 10^{-3}\ s^{-1}$. The Young's modulus of vertical Te nanowires was measured as $E_r = 73.64$ GPa, matching the simulation results (60 GPa).

Te nanomaterial–based nanogenerators

Three different Te nanomaterials, including vertical self-strained Te, horizontal unstrained Te, and vertical unstrained Te, were used as the active layer of nanogenerators. The vertical, self-strained, and unstrained Te nanomaterials were directly synthesized on a Au-coated polyethylene terephthalate (PET) flexible substrate. The gold layer coated on the PET flexible substrate serves as the bottom electrode and catalyst to boost the synthesis of Te nanomaterials. The horizontal unstrained Te was first synthesized on a mica substrate and then transferred to a gold-coated PET flexible substrate using a polymer-based wet-transfer method. Subsequently, a PPMA layer was spin-coated on the surface of the Te nanomaterials to act as an insulating layer, preventing electron leakage at the electrode/Te nanomaterials interface. Afterward, a 150-nm Au layer was deposited on the PMMA surface as the top electrode. In the end, a polydimethylsiloxane (PDMS) elastomeric layer was spin-coated to encapsulate the devices and enhance their structural stability. Experimentally, the periodic compressive stresses were perpendicularly applied to the Te active layers of nanogenerators using a customized bending and compressing system. The corresponding outputs were acquired through an oscilloscope (Tektronix, TBS1102B) equipped with a current preamplifier (SRS, SR570). Theoretically, the output difference between vertically self-strained Te and unstrained Te-based nanogenerators was simulated using COMSOL Multiphysics. To compute the electrical potential and peak voltage generated in vertically self-strained Te and unstrained Te responding to applied forces, the corresponding 2D models were built using COMSOL Multiphysics. In the simulation test, a time-varying vertical force was applied to the top of the model, and the corresponding surface potential and peak voltage were analyzed.

GPA and polarization vector map

The magnitude and distribution of strain inside Te nanomaterials were obtained by extracting the real-space and Fourier-space information of the HRTEM and HAADF-STEM images using strain ++ software. The strength of spontaneous polarization is linearly proportional to atomic displacement, i.e., $P_s \propto \Delta z$, where P_s is the spontaneous polarization and Δz is the magnitude of the displacement. Therefore, the local polarization and polarization vector map can be quantitatively assessed by measuring atomic displacement. The precise coordinates of each atom in the HAADF-STEM images were simulated using an efficient model-based estimation algorithm from

StatSTEM (*39*, *40*). The mean value of the off distance between the center atom and two side atoms over 256 unit cells at the unstrained top part was calculated and used as the reference. The magnitude of atomic displacement of center atoms at the self-strained tip was precisely calculated compared with this reference.

Thickness-dependent coercive field of Te

The measured coercive field at different thicknesses (E_m), when accounting for the depolarization field, can be expressed as follows (*46*, *50*)

$$E_m = E_c - E_{dep}$$

where E_{dep} is the thickness-dependent depolarization field, and E_c refer to the Janovec-Kay-Dunn (JKD) scaling relationship between coercive field and thickness that can be written as

$$E_c = k \times d^{-\frac{2}{3}}$$

$$E_{dep} = \frac{8\pi P_s \lambda}{\epsilon_e d}$$

Here, d is the thickness and k is the material specified. P_s is the spontaneous polarization, λ is the screening length and ϵ_e is the dielectric constant of the electrode.

Polarization reversal modulated conductance in FTJs

In this work, an ultrathin Te ferroelectric layer was adopted as the barrier layer, a Au layer coated on a silicon substrate served as the bottom electrode, and a conductive PtIr-coated AFM tip was used as the top electrode to construct a typical metal/ferroelectric/metal (M/F/M) asymmetry FTJ. The potential barrier for electron tunneling in this Te-based FTJ that takes the depolarization field into consideration can be described below (*46*, *50*)

$$\phi(x) = \begin{cases} \phi_0 - e\mathcal{E}_{dep}(t-\Delta t)x/\Delta t & \text{at } 0 \le x \le \Delta t \\ \phi_0 + e\mathcal{E}_{dep}(x_3 - t) & \text{at } \Delta t \le x \le t \end{cases}$$

where t is the barrier thickness and ϕ_0 is the barrier height at the original state that is not influenced by applied strain and depolarization field. Δt is the interfacial layer thickness, and $\mathcal{E}_{dep}$ is the depolarization field that is proportional to out-of-plane polarization, shown below

$$\mathcal{E}_{dep} \cong -P_s / \left[c_i(t-\Delta t) + \varepsilon_0 \varepsilon_f\right]$$

where P_s is the magnitude of spontaneous polarization in the absence of a depolarization field, c_i is the capacitance density, and ε_0 and ε_f is the permittivity of the vacuum and the relative out-of-plane permittivity of the barrier layer, respectively.

The mean barrier height $\bar{\phi}$ is obtained by the integration of $\phi(x)$

$$\bar{\phi} = \phi_0 + \frac{1}{2}e(t-\Delta t)\mathcal{E}_{dep} \cong \phi_0 - \frac{1}{2}\frac{eP_s}{\left[c_i + \frac{\varepsilon_0 \varepsilon_f}{t-\Delta t}\right]}$$

Thus, the modified magnitude of the mean barrier height by inhomogeneous strain-induced polarization reversal can be described as follows

$$2\Delta\bar{\phi} \cong \frac{e\,|P_s|\,(t-\Delta t)}{\left[c_i(t-\Delta t) + \varepsilon_0 \varepsilon_f\right]}$$

In the case of a Te-based FTJ, assuming $t = 3.5$ nm, $\Delta t \ll t$, $P_s = 0.5$ C/m^2, $c_i = 0.5$ F/m^2, and $\varepsilon_f < 300$, we obtain the change in the amount of the mean barrier height $\Delta\phi > 0.1$ eV. This change in the mean barrier height significantly affects the tunnel current, meaning that the inhomogeneous strain-induced polarization reversal notably influences the conductance of FTJs.

DFT computation details

The structural and electrical properties of the system were computed by using spin-polarized DFT as implemented in the Vienna ab initio simulation package (VASP 6.4) (*51*–*53*). A generalized gradient approximation with Perdew-Burke-Ernzerhof (PBE) functional was selected to describe the exchange-correlation interaction (*54*). The ion-electron interaction was characterized by the projector augmented wave method with a kinetic energy cutoff of 400 eV. Van der Waals interactions were accounted for using Grimme's DFT-D3 method (*55*). All the DFT calculations were carried out until the total energy and force were less than 10^{-5} eV per atom and 0.01 eV Å^{-1}, respectively. For sampling the Brillouin zone, a Monkhorst-Pack grid of $12 \times 12 \times 12$ K-point was used to optimize the lattice constants and atomic positions. To explore the flexoelectric tensor, the Brillouin zone integration was sampled using $6 \times 2 \times 2$ Monkhorst-Pack K-grids for the transverse model and $6 \times 6 \times 1$ for the longitudinal and shear model, respectively. The dielectric constant and the Born effective charges were calculated using the density functional perturbation theory (*56*–*58*). The local polarization of a unit cell in direction i ($i = x, y, z$)

$$P_i = \frac{1}{V}\sum_j w_j Z_j^* D_j \quad (1)$$

where V is the unit cell volume, w_j is the number of unit cells that share the atom, D_j is the atomic displacement vector from the ideal lattice site of atom j, and Z_j^* is the Born effective charge tensor. Index j runs over all atoms in the unit cell. Given that the PBE function generally underestimates the bandgap of semiconductors, a more accurate functional Heyd-Scuseria-Ernzerhof (HSE06) was used to calculate the bandgap of Te (*59*, *60*) (fig. S27). The Lobster software was used to perform the crystal orbital Hamilton population analysis to obtain the bonding and antibonding information (*61*). The spontaneous electric polarization of Te was predicted using the modern Berry phase method (*62*).

Theoretical simulations of the strain distributions

The Hertz contact mechanics of a spherical indenter were used to calculate Te bulk's strain distribution and strain gradient under a mechanically loaded tip-force model (*63*). The normal pressure distribution beneath a spherical indenter in a cylindrical coordinate system can be obtained by Eqs. 2 to 8

$$\frac{\sigma_{rr}}{p_m} = \frac{3}{2}\left\{\frac{1-2\upsilon}{3}\frac{a^2}{r^2}\left[1-\left(\frac{z}{u^{\frac{1}{2}}}\right)^3\right] + \left(\frac{z}{u^{\frac{1}{2}}}\right)^3 \frac{a^2 u}{u^2+a^2z^2} + \frac{z}{u^{\frac{1}{2}}}\left[u\frac{1-\nu}{a^2+u} + (1+\nu)\frac{u^{\frac{1}{2}}}{a}\tan^{-1}\left(\frac{a}{u^{\frac{1}{2}}}\right) - 2\right]\right\} \quad (2)$$

$$\frac{\sigma_{\theta\theta}}{p_m} = -\frac{3}{2}\left\{\frac{1-2\upsilon}{3}\frac{a^2}{r^2}\left[1-\left(\frac{z}{u^{\frac{1}{2}}}\right)^3\right] + \frac{z}{u^{\frac{1}{2}}}\left[2\nu + u\frac{1-\nu}{a^2+u} - (1+\nu)\frac{u^{\frac{1}{2}}}{a}\tan^{-1}\left(\frac{a}{u^{\frac{1}{2}}}\right)\right]\right\} \quad (3)$$

$$\frac{\sigma_{zz}}{p_m} = -\frac{3}{2}\left(\frac{z}{u^{\frac{1}{2}}}\right)^3 \frac{a^2 u}{u^2 + a^2 z^2} \tag{4}$$

$$a = \left[\frac{3}{4}\frac{F_l R}{Y}\left(1-\nu^2\right)\right]^{\frac{1}{3}} \tag{5}$$

$$p_m = \frac{F_l}{\pi a^2} \tag{6}$$

$$u = \frac{1}{2}\left\{\left(r^2+z^2-a^2\right) + \left[\left(r^2+z^2-a^2\right)^2 + az^2\right]^{\frac{1}{2}}\right\} \tag{7}$$

$$\frac{1}{Y} = \frac{1-\nu^2}{Y_{\mathrm{Te}}} + \frac{1-{\nu_{\mathrm{T}}}^2}{Y_{\mathrm{T}}} \tag{8}$$

where r, z, and θ are cylindrical coordinates, a is the radius of the contact area, σ is the stress, p_m is the mean pressure on the contact area, $F_l = 800$ nN is the tip loading force, and $R = 20$ nm is the radius of the silicon tip. $\nu = 0.228$ and $Y_{\mathrm{Te}} = 36.688$ GPa are Poisson's ratio and Young's modulus for Te, respectively. The silicon tip is considered a rigid hemisphere, and the Poisson's ratio and Young's modulus are $\nu_{\mathrm{T}} = 0.200$ and $Y_{\mathrm{T}} = 180.000$ GPa, respectively. With Hooke's law, the strain distribution can be calculated by

$$\varepsilon_{rr} = \frac{1}{E}\left[\sigma_{rr} - \nu\left(\sigma_{zz} + \sigma_{\theta\theta}\right)\right] \tag{9}$$

$$\varepsilon_{zz} = \frac{1}{E}\left[\sigma_{zz} - \nu\left(\sigma_{rr} + \sigma_{\theta\theta}\right)\right] \tag{10}$$

$$\varepsilon_{\theta\theta} = \frac{1}{E}\left[\sigma_{\theta\theta} - \nu\left(\sigma_{rr} + \sigma_{zz}\right)\right] \tag{11}$$

Theoretical simulations of the flexoelectric polarization

To investigate the coupling effects between the polarization and the strain gradient, direct flexoelectric polarization distributions of Te under an AFM tip force can be expressed by (*64*)

$$P_i = u_{ijkl}\frac{\partial \varepsilon_{kl}}{\partial x_j} \tag{12}$$

where P_i is the local polarization of a unit cell in direction i ($i = x, y, z$), u_{ijkl} is the flexoelectric coefficient (where j, k, and l also represent x, y, and z directions), and $\frac{\partial \varepsilon_{kl}}{\partial x_j}$ is the strain gradient (where x_j represents x, y, and z coordinates). In Eq. 12, the Einstein summation convention is used. The flexoelectric coefficients of Te in the longitudinal (u_{xxxx}, u_{yyyy}, and u_{zzzz}), transverse (u_{xxyy}, u_{yyxx}, u_{xxzz}, u_{zzxx}, u_{yyzz}, and u_{zzyy}), and shear directions (u_{xyxy}, u_{xzxz}, u_{yxyx}, u_{yzyz}, u_{zxzx}, and u_{zyzy}) are calculated by using the VASP, and the values are as follows: −30.57, 14.75, 60.93, 35.81, 36.99, 31.76, 13.07, −14.15, −18.12, 1.43, −0.67, 1.39, 0.14, −0.78, and 0.19 nC/m, respectively.

It is important to note that the precise values of the flexoelectric coefficients u_{ijkl} are unknown due to the difficulties in experimentally extracting them. As a result, there may be discrepancies between experimental and theoretical values for various reasons (*18*, *65*, *66*). Furthermore, it is worth noting that a hidden symmetry was proposed in the flexoelectric tensor, which further reduces the number of independent coefficients (*67*). The electric field can be calculated by

$$E = \frac{P}{\varepsilon_{\mathrm{r}}} \tag{13}$$

where P is the polarization and ε_{r} is the relative dielectric constant obtained from the density functional perturbation theory.

Supplementary Materials

The PDF file includes:

Tables S1 to S4
Figs. S1 to S55
Supplementary Notes S1 to S4
Legends for movies S1 and S2
References

Other Supplementary Material for this manuscript includes the following:

Movies S1 and S2

REFERENCES AND NOTES

1. R. Bian, R. He, E. Pan, Z. Li, G. Cao, P. Meng, J. Chen, Q. Liu, Z. Zhong, W. Li, F. Liu, Developing fatigue-resistant ferroelectrics using interlayer sliding switching. *Science* **385**, 57–62 (2024).
2. D. Zhang, P. Schoenherr, P. Sharma, J. Seidel, Ferroelectric order in van der Waals layered materials. *Nat. Rev. Mater.* **8**, 25–40 (2023).
3. Y. Li, J. Fu, X. Mao, C. Chen, H. Liu, M. Gong, H. Zeng, Enhanced bulk photovoltaic effect in two-dimensional ferroelectric $CuInP_2S_6$. *Nat. Commun.* **12**, 5896 (2021).
4. H. Ning, Z. Yu, Q. Zhang, H. Wen, B. Gao, Y. Mao, Y. Li, Y. Zhou, Y. Zhou, J. Chen, L. Liu, W. Wang, T. Li, Y. Li, W. Meng, W. Li, Y. Li, H. Qiu, Y. Shi, Y. Chai, H. Wu, X. Wang, An in-memory computing architecture based on a duplex two-dimensional material structure for in situ machine learning. *Nat. Nanotechnol.* **18**, 493–500 (2023).
5. L. Li, S. Zhao, W. Ran, Z. Li, Y. Yan, B. Zhong, Z. Lou, L. Wang, G. Shen, Dual sensing signal decoupling based on tellurium anisotropy for VR interaction and neuro-reflex system application. *Nat. Commun.* **13**, 5975 (2022).
6. Y. Meng, X. Li, X. Kang, W. Li, W. Wang, Z. Lai, W. Wang, Q. Quan, X. Bu, S. Yip, P. Xie, D. Chen, D. Li, F. Wang, C. Yeung, C. Lan, C. Liu, L. Shen, Y. Lu, F. Chen, C. Wong, J. C. Ho, Van der Waals nanomesh electronics on arbitrary surfaces. *Nat. Commun.* **14**, 2431 (2023).
7. C. Zhao, C. Tan, D. H. Lien, X. Song, M. Amani, M. Hettick, H. Y. Y. Nyein, Z. Yuan, L. Li, M. C. Scott, A. Javey, Evaporated tellurium thin films for p-type field-effect transistors and circuits. *Nat. Nanotechnol.* **15**, 53–58 (2020).
8. J. Chen, T. Zhang, J. Wang, L. Xu, Z. Lin, J. Liu, C. Wang, N. Zhang, S. P. Lau, W. Zhang, M. Chhowalla, Y. Chai, Topological phase change transistors based on tellurium Weyl semiconductor. *Sci. Adv.* **8**, eabn3837 (2022).
9. J. Shen, S. Jia, N. Shi, Q. Ge, T. Gotoh, S. Lv, Q. Liu, R. Dronskowski, S. R. Elliott, Z. Song, M. Zhu, Elemental electrical switch enabling phase segregation-free operation. *Science* **374**, 1390–1394 (2021).
10. G. Rao, H. Fang, T. Zhou, C. Zhao, N. Shang, J. Huang, Y. Liu, X. Du, P. Li, X. Jian, L. Ma, J. Wang, K. Liu, J. Wu, X. Wang, J. Xiong, Robust piezoelectricity with spontaneous polarization in monolayer tellurene and multilayer tellurium film at room temperature for reliable memory. *Adv. Mater.* **34**, e2204697 (2022).
11. L. Yang, S. Ding, J. Gao, M. Wu, Atypical sliding and Moiré ferroelectricity in pure multilayer graphene. *Phys. Rev. Lett.* **131**, 096801 (2023).
12. C. Xiao, F. Wang, S. A. Yang, Y. Lu, Y. Feng, S. Zhang, Elemental ferroelectricity and antiferroelectricity in Group-V monolayer. *Adv. Funct. Mater.* **28**, 1707383 (2018).
13. Y. Liang, R. Guo, S. Shen, B. Huang, Y. Dai, Y. Ma, Out-of-plane ferroelectricity and multiferroicity in elemental bilayer phosphorene, arsenene, and antimonene. *Appl. Phys. Lett.* **118**, 012905 (2021).
14. Y. Wang, C. Xiao, M. Chen, C. Hua, J. Zou, C. Wu, J. Jiang, S. A. Yang, Y. Lu, W. Ji, Two-dimensional ferroelectricity and switchable spin-textures in ultra-thin elemental Te multilayers. *Mater. Horiz.* **5**, 521–528 (2018).
15. J. Gou, H. Bai, X. Zhang, Y. L. Huang, S. Duan, A. Ariando, S. A. Yang, L. Chen, Y. Lu, A. T. S. Wee, Two-dimensional ferroelectricity in a single-element bismuth monolayer. *Nature* **617**, 67–72 (2023).

16. J. Zhang, J. Zhang, Y. Qi, S. Gong, H. Xu, Z. Liu, R. Zhang, M. A. Sadi, D. Sychev, R. Zhao, H. Yang, Z. Wu, D. Cui, L. Wang, C. Ma, X. Wu, J. Gao, Y. P. Chen, X. Wang, Y. Jiang, Room-temperature ferroelectric, piezoelectric and resistive switching behaviors of single-element Te nanowires. *Nat. Commun.* **15**, 7648 (2024).
17. Z. Zhang, L. Z. Yang, H. J. Qin, W. A. Liao, H. Liu, J. Fu, H. Zeng, W. Zhang, Y. S. Fu, Direct observations of spontaneous in-plane electronic polarization in 2D Te films. *Adv. Mater.* **36**, 2405590 (2024).
18. L. Wang, S. Liu, X. Feng, C. Zhang, L. Zhu, J. Zhai, Y. Qin, Z. L. Wang, Flexoelectronics of centrosymmetric semiconductors. *Nat. Nanotechnol.* **15**, 661–667 (2020).
19. S. Cai, Y. Lun, D. Ji, P. Lv, L. Han, C. Guo, Y. Zang, S. Gao, Y. Wei, M. Gu, C. Zhang, Z. Gu, X. Wang, C. Addiego, D. Fang, Y. Nie, J. Hong, P. Wang, X. Pan, Enhanced polarization and abnormal flexural deformation in bent freestanding perovskite oxides. *Nat. Commun.* **13**, 5116 (2022).
20. J. Jiang, M. Xiong, K. Fan, C. Bao, D. Xin, Z. Pan, L. Fei, H. Huang, L. Zhou, K. Yao, X. Zheng, L. Shen, F. Gao, Synergistic strain engineering of perovskite single crystals for highly stable and sensitive X-ray detectors with low-bias imaging and monitoring. *Nat. Photon.* **16**, 575–581 (2022).
21. L. Yang, S. Yue, Y. Tao, S. Qiao, H. Li, Z. Dai, B. Song, Y. Chen, J. Du, D. Li, P. Gao, Suppressed thermal transport in silicon nanoribbons by inhomogeneous strain. *Nature* **629**, 1021–1026 (2024).
22. W. Peng, S. Y. Park, C. J. Roh, J. Mun, H. Ju, J. Kim, E. K. Ko, Z. Liang, S. Hahn, J. Zhang, A. M. Sanchez, D. Walker, S. Hindmarsh, L. Si, Y. J. Jo, Y. Jo, T. H. Kim, C. Kim, L. Wang, M. Kim, J. S. Lee, T. W. Noh, D. Lee, Flexoelectric polarizing and control of a ferromagnetic metal. *Nat. Phys.* **20**, 450–455 (2024).
23. K. Chu, B. K. Jang, J. H. Sung, Y. A. Shin, E. S. Lee, K. Song, J. H. Lee, C. S. Woo, S. J. Kim, S. Y. Choi, T. Y. Koo, Y. H. Kim, S. H. Oh, M. H. Jo, C. H. Yang, Enhancement of the anisotropic photocurrent in ferroelectric oxides by strain gradients. *Nat. Nanotech.* **10**, 972–979 (2015).
24. J. Wang, L. He, Y. Zhang, H. Nong, S. Li, Q. Wu, J. Tan, B. Liu, Locally strained 2D materials: Preparation, properties, and applications. *Adv. Mater.* **36**, e2314145 (2024).
25. H. Lu, C. W. Bark, D. E. de los Ojos, J. Alcala, C. B. Eom, G. Catalan, A. Gruverman, Mechanical writing of ferroelectric polarization. *Science* **336**, 59–61 (2012).
26. J. H. Lee, H. J. Kim, J. Yoon, S. Kim, J. R. Kim, W. Peng, S. Y. Park, T. W. Noh, D. Lee, Flexoelectricity-driven mechanical switching of polarization in metastable ferroelectrics. *Phys. Rev. Lett.* **129**, 117601 (2022).
27. R. Xu, J. Huang, E. S. Barnard, S. S. Hong, P. Singh, E. K. Wong, T. Jansen, V. Harbola, J. Xiao, B. Y. Wang, S. Crossley, D. Lu, S. Liu, H. Y. Hwang, Strain-induced room-temperature ferroelectricity in $SrTiO_3$ membranes. *Nat. Commun.* **11**, 3141 (2020).
28. M. Wu, Z. Lou, C. M. Dai, T. Wang, J. Wang, Z. Zhu, Z. Xu, T. Sun, W. Li, X. Zheng, X. Lin, Achieving ferroelectricity in a centrosymmetric high-performance semiconductor by strain engineering. *Adv. Mater.* **35**, e2300450 (2023).
29. K. J. Choi, M. Biegalski, Y. L. Li, A. Sharan, J. Schubert, R. Uecker, P. Reiche, Y. B. Chen, X. Q. Pan, V. Gopalan, L. Q. Chen, D. G. Schlom, C. B. Eom, Enhancement of ferroelectricity in strained $BaTiO_3$ thin films. *Science* **306**, 1005–1009 (2004).
30. K. Shimizu, H. Hojo, Y. Ikuhara, M. Azuma, Enhanced piezoelectric response due to polarization rotation in cobalt-substituted $BiFeO_3$ epitaxial thin films. *Adv. Mater.* **28**, 8639–8644 (2016).
31. A. R. Damodaran, E. Breckenfeld, Z. Chen, S. Lee, L. W. Martin, Enhancement of ferroelectric curie temperature in $BaTiO_3$ films via strain-induced defect dipole alignment. *Adv. Mater.* **26**, 6341–6347 (2014).
32. G. Catalan, A. Lubk, A. H. G. Vlooswijk, E. Snoeck, C. Magen, A. Janssens, G. Rispens, G. Rijnders, D. H. A. Blank, B. Noheda, Flexoelectric rotation of polarization in ferroelectric thin films. *Nat. Mater.* **10**, 963–967 (2011).
33. H. Fu, R. E. Cohen, Polarization rotation mechanism for ultrahigh electromechanical response in single-crystal piezoelectrics. *Nature* **403**, 281–283 (2000).
34. F. Li, S. Zhang, T. Yang, Z. Xu, N. Zhang, G. Liu, J. Wang, J. Wang, Z. Cheng, Z. G. Ye, J. Luo, T. R. Shrout, L. Q. Chen, The origin of ultrahigh piezoelectricity in relaxor-ferroelectric solid solution crystals. *Nat. Commun.* **7**, 13807 (2016).
35. Y. Zhang, J. Mao, R. K. Zheng, J. Zhang, Y. Wu, X. Wang, K. Miao, H. Yao, L. Yang, H. Zheng, Ferroelectric polarization-enhanced performance of flexible $CuInP_2S_6$ piezoelectric nanogenerator for biomechanical energy harvesting and voice recognition applications. *Adv. Funct. Mater.* **33**, 2214745 (2023).
36. C. Shi, Z. Cheng, A. Leonardi, Y. Yang, M. Engel, M. R. Jones, Y. Han, Preserving surface strain in nanocatalysts via morphology control. *Sci. Adv.* **10**, eadp3788 (2024).
37. H. S. Shin, J. Yu, J. Y. Song, H. M. Park, Size dependence of lattice deformation induced by growth stress in Sn nanowires. *Appl. Phys. Lett.* **94**, 011906 (2009).
38. C. L. Jia, V. Nagarajan, J. Q. He, L. Houben, T. Zhao, R. Ramesh, K. Urban, R. Waser, Unit-cell scale mapping of ferroelectricity and tetragonality in epitaxial ultrathin ferroelectric films. *Nat. Mater.* **6**, 64–69 (2007).
39. P. Gao, A. Kumamoto, R. Ishikawa, N. Lugg, N. Shibata, Y. Ikuhara, Picometer-scale atom position analysis in annular bright-field STEM imaging. *Ultramicroscopy* **184**, 177–187 (2018).
40. A. D. Backer, K. H. W. van den Bos, W. V. den Broek, J. Sijbers, S. V. Aert, StatSTEM: An efficient approach for accurate and precise model-based quantification of atomic resolution electron microscopy images. *Ultramicroscopy* **171**, 104–116 (2016).
41. A. Chanthbouala, A. Crassous, V. Garcia, K. Bouzehouane, S. Fusil, X. Moya, J. Allibe, B. Dlubak, J. Grollier, S. Xavier, C. Deranlot, A. Moshar, R. Proksch, N. D. Mathur, M. Bibes, A. Barthélémy, Solid-state memories based on ferroelectric tunnel junctions. *Nat. Nanotech.* **7**, 101–104 (2012).
42. V. Garcia, M. Bibes, Ferroelectric tunnel junctions for information storage and processing. *Nat. Commun.* **5**, 4289 (2014).
43. S. Das, B. Wang, T. R. Paudel, S. M. Park, E. Y. Tsymbal, L. Q. Chen, D. Lee, T. W. Noh, Enhanced flexoelectricity at reduced dimensions revealed by mechanically tunable quantum tunnelling. *Nat. Commun.* **10**, 537 (2019).
44. X. Jiang, X. Wang, X. Wang, X. Zhang, R. Niu, J. Deng, S. Xu, Y. Lun, Y. Liu, T. Xia, J. Lu, J. Hong, Manipulation of current rectification in van der Waals ferroionic $CuInP_2S_6$. *Nat. Commun.* **13**, 574 (2022).
45. S. M. Park, B. Wang, S. Das, S. C. Chae, J. S. Chung, J. G. Yoon, L. Q. Chen, S. M. Yang, T. W. Noh, Selective control of multiple ferroelectric switching pathways using a trailing flexoelectric field. *Nat. Nanotech.* **13**, 366–370 (2018).
46. H. Kohlstedt, N. A. Pertsev, J. Rodríguez Contreras, R. Waser, Theoretical current-voltage characteristics of ferroelectric tunnel junctions. *Phys. Rev. B* **72**, 125341 (2005).
47. Y. Yan, W. G. Kim, X. Ma, T. Tegafaw, T. M. Nguyen, J. M. Lee, E. J. Choi, H. Ahn, S. H. Ha, K. Kim, J. M. Kim, H. K. Kim, J. W. Oh, D. M. Shin, Y. H. Hwang, Nanogenerators facilitated piezoelectric and flexoelectric characterizations for bioinspired energy harvesting materials. *Nano Energy* **81**, 105607 (2021).
48. Y. Yan, X. Ma, T. M. Nguyen, S. H. Ha, H. Ahn, D. Aben, K. Kim, J. M. Kim, J. W. Oh, D. M. Shin, Y. H. Hwang, Quadrant-electroded nanogenerators for decoupling piezoelectricity and flexoelectricity in the electromechanical outputs in flexible devices. *Nano Energy* **104**, 107909 (2022).
49. R. Gaillac, P. Pullumbi, F. X. Coudert, ELATE: An open-source online application for analysis and visualization of elastic tensors. *J. Phys. Condens. Matter* **28**, 275201 (2016).
50. A. Gruverman, D. Wu, H. Lu, Y. Wang, H. W. Jang, C. M. Folkman, M. Y. Zhuravlev, D. Felker, M. Rzchowski, C. B. Eom, E. Y. Tsymbal, Tunneling electroresistance effect in ferroelectric tunnel junctions at the nanoscale. *Nano Lett.* **9**, 3539–3543 (2009).
51. G. Kresse, J. Hafner, Ab initio molecular dynamics for liquid metals. *Phys. Rev. B Condens. Matter* **47**, 558–561 (1993).
52. G. Kresse, J. Furthmüller, Efficient iterative schemes for ab initio total-energy calculations using a plane-wave basis set. *Phys. Rev. B Condens. Matter.* **54**, 11169–11186 (1996).
53. G. Kresse, J. Furthmüller, Efficiency of ab-initio total energy calculations for metals and semiconductors using a plane-wave basis set. *Comput. Mater. Sci.* **6**, 15–50 (1996).
54. J. P. Perdew, K. Burke, M. Ernzerhof, Generalized gradient approximation made simple. *Phys. Rev. Lett.* **77**, 3865–3868 (1996).
55. S. Grimme, S. Ehrlich, L. Goerigk, Effect of the damping function in dispersion corrected density functional theory. *J. Comput. Chem.* **32**, 1456–1465 (2011).
56. S. Baroni, S. de Gironcoli, A. D. Corso, P. Giannozzi, Phonons and related crystal properties from density-functional perturbation theory. *Rev. Mod. Phys.* **73**, 515–562 (2001).
57. X. Gonze, C. Lee, Dynamical matrices, Born effective charges, dielectric permittivity tensors, and interatomic force constants from density-functional perturbation theory. *Phys. Rev. B* **55**, 10355–10368 (1997).
58. X. Gonze, First-principles responses of solids to atomic displacements and homogeneous electric fields: Implementation of a conjugate-gradient algorithm. *Phys. Rev. B* **55**, 10337–10354 (1997).
59. A. J. Garza, G. E. Scuseria, Predicting band gaps with hybrid density functionals. *J. Phys. Chem. Lett.* **7**, 4165–4170 (2016).
60. H. Xiao, J. Tahir-Kheli, W. A. Goddard III, Accurate band gaps for semiconductors from density functional theory. *J. Phys. Chem. Lett.* **2**, 212–217 (2011).
61. V. L. Deringer, A. L. Tchougreeff, R. Dronskowski, Crystal orbital Hamilton population (COHP) analysis as projected from plane-wave basis sets. *J. Phys. Chem. A* **115**, 5461–5466 (2011).
62. R. D. King-Smith, D. Vanderbilt, Theory of polarization of crystalline solids. *Phys. Rev. B* **47**, 1651–1654 (1993).
63. A. C. Fischer-Cripps, *Introduction to Contact Mechanics* (Springer, 2007).
64. P. V. Yudin, A. K. Tagantsev, Fundamentals of flexoelectricity in solids. *Nanotechnology* **24**, 432001 (2013).
65. J. Narvaez, F. V. Sancho, G. Catalan, Enhanced flexoelectric-like response in oxide semiconductors. *Nature* **538**, 219–221 (2016).
66. J. Hong, D. Vanderbilt, First-principles theory and calculation of flexoelectricity. *Phys. Rev. B* **88**, 174107 (2013).
67. E. A. Eliseev, A. N. Morozovska, Hidden symmetry of flexoelectric coupling. *Phys. Rev. B* **98**, 094108 (2018).
68. Y. Hu, C. Xu, Y. Zhang, L. Lin, R. L. Snyder, Z. L. Wang, A nanogenerator for energy harvesting from a rotating tire and its application as a self-powered pressure/speed sensor. *Adv. Mater.* **35**, 4068–4071 (2011).

69. S. Xu, Y. Qin, C. Xu, Y. Wei, R. Yang, Z. L. Wang, Self-powered nanowire devices. *Nat. Nanotechnol.* **5**, 366–373 (2010).
70. Z. W. Pan, Z. R. Dai, Z. L. Wang, Nanobelts of semiconducting oxides. *Science* **291**, 1947–1949 (2001).
71. R. Yang, Y. Qin, L. Dai, Z. L. Wang, Power generation with laterally packaged piezoelectric fine wires. *Nat. Nanotechnol.* **4**, 34–39 (2009).
72. P. C. Chang, Z. Fan, D. Wang, W. Y. Tseng, W. A. Chiou, J. H. Jia, G. Lu, ZnO nanowires synthesized by vapor trapping CVD method. *Chem. Mater.* **16**, 5133–5137 (2004).
73. I. Boukhoubza, E. Matei, A. Jorio, M. Enculescu, I. Enculescu, Electrochemical deposition of ZnO nanowires on CVD-graphene/copper substrates. *Nanomaterials* **12**, 2858 (2022).
74. S. Xu, G. Poirier, N. Yao, PMN-PT nanowires with a very high piezoelectric constant. *Nano Lett.* **12**, 2238–2242 (2012).
75. A. Koka, Z. Zhoub, H. A. Sodano, Vertically aligned $BaTiO_3$ nanowire arrays for energy harvesting. *Energ. Environ. Sci.* **7**, 288–296 (2014).
76. N. Gogneau, P. Chrétien, E. Galopin, S. Guilet, L. Travers, J. C. Harmand, F. Houzé, Impact of the GaN nanowire polarity on energy harvesting. *Appl. Phys. Lett.* **104**, 213105 (2014).
77. X. Chen, S. Xu, N. Yao, Y. Shi, 1.6 V nanogenerator for mechanical energy harvesting using PZT nanofibers. *Nano Lett.* **10**, 2133–2137 (2010).
78. C. T. Huang, J. Song, C. M. Tsai, W. F. Lee, D. H. Lien, Z. Gao, Y. Hao, L. Chen, Z. L. Wang, Single-InN-nanowire nanogenerator with upto 1 V output voltage. *Adv. Mater.* **22**, 4008–4013 (2010).
79. J. M. Wu, C. C. Kaob, Self-powered pendulum and micro-force active sensors based on a ZnS nanogenerator. *RSC Adv.* **4**, 13882–13887 (2014).
80. M. Wu, Y. Wang, S. Gao, R. Wang, C. Ma, Z. Tang, N. Bao, W. Wu, F. Fan, W. Wu, Solution-synthesized chiral piezoelectric selenium nanowires for wearable self-powered human-integrated monitoring. *Nano Energy* **56**, 693–699 (2019).
81. T. I. Lee, S. Lee, E. Lee, S. Sohn, Y. Lee, S. Lee, G. Moon, D. Kim, Y. S. Kim, J. M. Myoung, Z. L. Wang, High-power density piezoelectric energy harvesting using radially strained ultrathin trigonal tellurium nanowire assembly. *Adv. Mater.* **25**, 2920–2925 (2013).
82. X. D. Bai, P. X. Gao, Z. L. Wang, E. G. Wang, Gal-mode mechanical resonance of individual ZnO nanobelts. *Appl. Phys. Lett.* **82**, 4806–4808 (2003).
83. J. Song, X. Wang, E. Riedo, Z. L. Wang, Elastic property of vertically aligned nanowires. *Nano Lett.* **5**, 1954–1958 (2005).
84. Y. Huang, X. Bai, Y. Zhang, In situ mechanical properties of individual ZnO nanowires and the mass measurement of nanoparticles. *J. Phys. Condens. Matter* **18**, 179–184 (2006).
85. B. Moorthy, C. Baek, J. E. Wang, C. K. Jeong, S. Moon, K. I. Park, D. K. Kim, Piezoelectric energy harvesting from a PMN–PT single nanowire. *RSC Adv.* **7**, 260–265 (2017).
86. S. Dai, J. Zhao, M. He, X. Wang, J. Wan, Z. Shan, J. Zhu, Elastic properties of GaN nanowires: Revealing the influence of planar defects on Young's modulus at nanoscale. *Nano Lett.* **15**, 8–15 (2015).
87. X. Chen, S. Xu, N. Yao, Y. Shi, Young's modulus determination of unpolled electrospun PZT nanofibers. *Sci. Adv. Mater.* **4**, 847–850 (2012).
88. X. Li, X. Wang, Q. Xiong, P. C. Eklund, Mechanical properties of ZnS nanobelts. *Nano Lett.* **5**, 1982–1986 (2005).
89. Q. Xiong, N. Duarte, S. Tadigadapa, P. C. Eklund, Force-deflection spectroscopy: A new method to determine the Young's modulus of nanofilaments. *Nano Lett.* **6**, 1904–1909 (2006).
90. M. M. Jolandan, R. A. Bernal, I. Kuljanishvili, V. Parpoil, H. D. Espinosa, Individual GaN nanowires exhibit strong piezoelectricity in 3D. *Nano Lett.* **12**, 970–976 (2012).
91. J. Wang, C. Stampfer, C. Roman, W. H. Ma, N. Setter, C. Hierold, Piezoresponse force microscopy on doubly clamped $KNbO_3$ nanowires. *Appl. Phys. Lett.* **93**, 223101 (2008).
92. T. Y. Ke, H. A. Chen, H. S. Sheu, J. W. Yeh, H. N. Lin, C. Y. Lee, H. T. Chiu, Sodium niobate nanowire and its piezoelectricity. *J. Phys. Chem. C* **112**, 8827–8831 (2008).
93. Z. Wang, J. Hu, M. F. Yu, Axial polarization switching in ferroelectric $BaTiO_3$ nanowire. *Nanotechnology* **18**, 235203 (2007).
94. J. Zhu, L. Jia, R. Huang, Electrospinning poly(L-lactic acid) piezoelectric ordered porous nanofibers for strain sensing and energy harvesting. *J. Mater. Sci. Mater. Electron.* **28**, 12080–12085 (2017).
95. S. Anwar, M. H. Amiri, S. Jiang, M. M. Abolhasani, P. R. F. Rocha, K. Asadi, Piezoelectric nylon-11 fibers for electronic textiles, energy harvesting and sensing. *Adv. Funct. Mater.* **31**, 2004326 (2021).
96. S. Bodkhe, G. Turcot, F. P. Gosselin, D. Therriault, One-step solvent evaporation-assisted 3D printing of piezoelectric PVDF nanocomposite structures. *ACS Appl. Mater. Interfaces* **9**, 20833–20842 (2017).
97. D. M. Shin, H. J. Han, W. G. Kim, E. Kim, C. Kim, S. W. Hong, H. K. Kim, J. W. Oh, Y. H. Hwang, Bioinspired piezoelectric nanogenerators based on vertically aligned phage nanopillars. *Energ. Environ. Sci.* **8**, 3198–3203 (2015).
98. H. Y. Son, S. S. Park, Collagen-based biopiezoelectric nanogenerator prepared from pollack skin. *Mater. Today Sustain.* **25**, 100689 (2024).
99. M. T. Chorsi, E. J. Curry, H. T. Chorsi, R. Das, J. Baroody, P. K. Purohit, H. Ilies, T. D. Nguyen, Piezoelectric biomaterials for sensors and actuators. *Adv. Mater.* **31**, e1802084 (2019).

Acknowledgments: We sincerely thank H. Hu from Oxford Instruments (Beijing) for invaluable contributions to SHG measurements. We are thankful to B. Liu and Y. Zhang at Tsinghua Shenzhen International Graduate School, Tsinghua University, for assistance with the DART-SS PFM experiments. In addition, we acknowledge the significant contributions and professional technical support of H. Li from Bruker Instruments to the PFM measurements. We also thank R. Zhu from Oxford Instruments for expertise and support in the PFM and CAFM measurements. **Funding:** This research was financially supported by the Research Grants Council of the Hong Kong Special Administrative Region, China (CRS_CityU101/24), the Innovation and Technology Fund (MHP/044/23) from the Innovation Technology Commission of the Hong Kong Special Administrative Region, China, the Science Technology and Innovation Committee of Shenzhen Municipality (JCYJ20230807114910021), and Guangdong Basic and Applied Basic Research Foundation (2024A1515011922). X.L. and X.C.Z. acknowledges the Guangdong Basic and Applied Basic Research Foundation (2023A1515110920 and 2024A1515012307) and the Sichuan Science and Technology Program (2024NSFSC1141). Y.L. acknowledges support by the Hong Kong RGC general research fund (RFS2021-1S05 and T45-406/23-R). **Author contributions:** Y. Yan, Y.M., and J.C.H. conceived the study and designed the experiments. Y. Yan and Y.M. carried out the sample preparation, AFM and PFM characterization, and device fabrication. X.L. and X.C.Z. contributed to first-principles calculations, and L.W. and Y.L. contributed to the TEM characterization, GPA, and nanoindentation. Y. Zhang performed DFT calculations. J.Z. and D.-M.S. contributed to the COMSOL Multiphysics simulation. Z.Z. and Y. Yang contributed to CAFM measurements. Y. Zhou and Z.F. contributed to ion milling and SEM characterization. I.F. and W.A.D. contributed to nanogenerators' performance measurements. Y.X. contributed to SEM characterization. Weijun W., Z.L., Wei W., P.X., W.A.D., D.-M.S., Z.F., Y. Yang, Y.L., and X.C.Z. contributed to the data analysis. Y. Yan, X.C.Z., Y.M., and J.C.H. wrote and revised the manuscript. **Competing interests:** The authors declare that they have no competing interests. **Data and materials availability:** All data needed to evaluate the conclusions in the paper are present in the paper and/or the Supplementary Materials.

Submitted 26 October 2024
Accepted 26 June 2025
Published 1 August 2025
10.1126/sciadv.adu1716